Journal of Alloys and Compounds 968 (2023) 172027

Contents lists available at ScienceDirect

Journal of Alloys and Compounds

journal homepage: www.elsevier.com/locate/jalcom

Reversible Fe^{3+}/Fe^{2+} and Ti^{4+}/Ti^{3+} redox couple in Fe-substituted $LiTi_2O_4$ ramsdellite and its electrochemical properties as electrode material in lithium ion batteries

Pilar Díaz-Carrasco [a], Alois Kuhn [a,*], Nieves Menéndez [b], Flaviano García-Alvarado [a]

[a] Departamento de Química y Bioquímica, Facultad de Farmacia, Universidad San Pablo-CEU, CEU Universities, Urbanización Montepríncipe, Boadilla del Monte, Madrid 28668, Spain
[b] Departamento de Química Física Aplicada, Facultad de Ciencias, Universidad Autónoma de Madrid, 28049 Madrid, Spain

ARTICLE INFO

Keywords:
Lithium titanate
Ramsdellite
^{57}Fe Mössbauer spectroscopy
Anode
Lithium ion battery

ABSTRACT

Ti/Fe substitution in ramsdellite $LiTi_2O_4$, an attractive insertion material for lithium-ion battery applications, has been performed by the ceramic method yielding electrode materials with general stoichiometry $LiFe_xTi_{2-x}O_4$. Samples with $0 \leq x \leq 0.5$ resulted in well crystallized orthorhombic ramsdellite phases, space group *Pbnm*, while samples with $x > 0.5$ formed spinel, space group *Fd-3m*, as revealed by powder X-ray diffraction. The ramsdellites were further investigated with X-EDS microanalysis, ^{57}Fe Mössbauer spectroscopy and electrochemical discharge-charge cycling in lithium cells. This provided a comprehensive insight into the Ti/Fe substitution mechanism, which turned out to be rather more complex than the predicted simple M^{3+} isovalent substitution, with participation of Fe^{3+}/Fe^{2+} and Ti^{4+}/Ti^{3+}. Upon testing against lithium in the low voltage range (*ocv*-1 V), ramsdellite with low Ti/Fe substitution, namely $LiFe_{0.125}Ti_{1.875}O_4$, outperformed undoped $LiTi_2O_4$ electrochemically, delivering a 1st cycle capacity of 180 mAh g^{-1} at C/30 (5.3 mA g^{-1}) stabilized at 140 mAh g^{-1} upon cycling, compared to 120 and 80 mAh g^{-1}, respectively, in $LiTi_2O_4$. Two active redox pairs, Ti^{4+}/Fe^{3+} and Fe^{3+}/Fe^{2+}, combined with better electrical properties due to the presence of metallic iron, boosting farther electronic conductivity in $LiFe_{0.125}Ti_{1.875}O_4$, allow a noticeable capacity of 71 mAh g^{-1} still to be held at a high current of 2 C (320 mA g^{-1}). In the high voltage range (*ocv*-4 V), $LiFe_{0.125}Ti_{1.875}O_4$ electrochemically outmatched the higher Fe-substituted ramsdellites, which were characterized by a high irreversible capacity ascribed to the unavailability of Fe^{3+}/Fe^{4+} redox couple and electrolyte decomposition.

1. Introduction

Titanium-based oxides have been widely investigated as negative electrode materials for lithium ion batteries and some of them successfully commercialized (e.g. Altairnano, Microvast, Log9, Toshiba, YABO, Yinlong Energy). Besides affordable price, widespread natural sources subsequently bypassing political risk, and non-toxicity, the great interest of this type of materials is a low intercalation voltage, at ~1.5 V owed to the electroactive Ti^{4+}/Ti^{3+} redox couple, low enough to be competitive as the negative electrode but high enough to make batteries safer avoiding lithium plating and concomitant risks. All of which explains why their investigation continues to be headline in the field with many structural types and morphologies being electrochemically active [1–3]: TiO_2 phases such as nanostructured anatase [4], rutile [5,6], hollandite [7], ramsdellite [8], bronze-type TiO_2(B) [9], and further spinels $Li_4Ti_5O_{12}$ [10–12], $LiCrTiO_4$ [13,14], $LiFeTiO_4$/CNTs [15], and ramsdellite $Li_2Ti_3O_7$ [16] have been investigated as prospective negative electrodes for safe Li-ion batteries [17,18]. Ramsdellite $LiTi_2O_4$ enables both lithium insertion and deinsertion due to the mixed titanium oxidation state ($LiTi^{3+}Ti^{4+}O_4$) [19,20]. Thus, lithium deinsertion from ramsdellite $LiTi_2O_4$ at potentials from 1.8 to 2.5 V with oxidation of all Ti^{3+} to Ti^{4+} produces Ti_2O_4, this is the TiO_2 ramsdellite polymorph, whereas lithium insertion into $LiTi_2O_4$ ramsdellite at potentials from 1.8 to 1.0 V with reduction of all Ti^{4+} to Ti^{3+} produces $Li_2Ti_2O_4$. Both deinsertion and insertion processes in $LiTi_2O_4$ develop a theoretical capacity of 161 mAh g^{-1}, while a total theoretical capacity of 336 mAh g^{-1} in the full potential range 1.0–2.5 V is achieved considering the lithium-deinserted TiO_2 ramsdellite [8,21].

* Corresponding author.
E-mail address: akuhn@ceu.es (A. Kuhn).

https://doi.org/10.1016/j.jallcom.2023.172027
Received 28 April 2023; Received in revised form 6 August 2023; Accepted 3 September 2023
Available online 8 September 2023

The Ti^{4+}/Ti^{3+} redox couple generally displays an insufficiently low potential for cathode applications, thus being mostly employed to build negative electrode materials.

Nevertheless, replacing Ti^{3+} by metals with a higher M^{n+1}/M^{n+} potential is a straightforward strategy to a dual electrode with Ti^{4+}/Ti^{3+} reductive insertion of Li as anode and M^{n+1}/M^{n+} oxidative deinsertion of Li as the cathode displayed by the same material. In particular, this strategy has been successfully demonstrated in 1:1 ramsdellites $LiTiVO_4$ and $LiCrTiO_4$ [22,23] with electrochemical Li^+ deinsertion potentials of 3.1 V for reversible V^{4+}/V^{3+} [24] and very high 4.0 V ascribed to reversible Cr^{4+}/Cr^{3+} transitions, unlocking its potential as a dual electrode [23]. Computational results indicate that for $LiTiMO_4$ (M= Ti, V, Cr, Mn and Fe) [25] the spinel structure is thermodynamically favored with respect to the ramsdellite polymorph, and the spinel to ramsdellite transformation temperature was estimated theoretically to lie in the range 900–1600 ºC for Ti, V, and Cr. Consistent with this, Ti, V and Cr containing ramsdellite phases [22–26] were experimentally confirmed by heat treatment of the corresponding spinel phases in the temperature range 900–1400 ºC followed by final quenching. However, owing to a significant degree of inversion in spinels $LiMTiO_4$ with M= Mn and Fe, and according to computational studies, the ramsdellite phase was expected to be stabilized at much higher temperature (T > 1600 ºC) well beyond the melting point of the corresponding spinel phases. Therefore, ramsdellites $LiMnTiO_4$ and $LiFeTiO_4$ have not been reported so far. There are evidences that lowering iron content in $LiFe_xTi_{2-x}O_4$ (x < 1) allows formation of the ramsdellite phase at lower temperature without melting as it is the case of $LiTi_{1.5}Fe_{0.5}O_4$ [27]. However, there has been no systematic study of the $LiTi_{2-x}Fe_xO_4$ system in the compositional range 0 < x < 1 to date. Furthermore, the role the two active redox couples, Ti^{4+}/Ti^{3+} and Fe^{3+}/Fe^{2+}, may play on electrochemical Li insertion and deinsertion properties have remained completely unexplored.

In this work, we focus on the effects of substituting nominally Ti^{3+} by Fe^{3+} in ramsdellite $LiTi_2O_4$ leading to Fe-substituted ramsdellites $LiFe_xTi_{2-x}O_4$ ($0 < x \leq 0.5$). We report on preparation details, crystal structure, oxidation state of iron in as-prepared electrode materials as deduced from ^{57}Fe Mössbauer spectroscopy and provide cycling performances in lithium cells. Electrochemical results are compared with bare $LiTi_2O_4$ revealing a significant improvement of capacity for low iron content.

2. Experimental

2.1. Synthesis of $LiFe_xTi_{2-x}O_4$ compounds

$LiFe_xTi_{2-x}O_4$ compounds with nominal compositions x = 0, 0.125, 0.25, 0.5, 0.75 and 1 were prepared in two steps according to the general reaction:

$$Li_2CO_3 + (1\text{-}x)\ Ti_2O_3 + 2\ TiO_2 + x\ Fe_2O_3 \rightarrow 2\ LiFe_xTi_{2-x}O_4 + CO_2 \quad (1)$$

First a mixture of the stoichiometric amount of the air stable reagents Li_2CO_3, TiO_2 (anatase) and Fe_2O_3 were pelletized and heated at 800º C for 12 h. The resulting product was then mixed with Ti_2O_3 in an Argon filled glove box and pelletized. For compositions x = 0, 0.125 pellets were wrapped in copper foil, after sealed in evacuated silica ampoules and heated at 1000 ºC (x = 0) and 1010 ºC (x = 0.125). For compositions x = 0.25, 0.5 and 0.75, mixtures were heated in arc-welded platinum tubes at 1250 ºC (x = 0.25, 0.5) and 1275 ºC (x = 0.75) Finally, composition x = 1 was obtained by heating the mixture of air-stable reactants at 1400 ºC in an alumina crucible in air. For iron-substituted compounds, melting occurred at temperatures higher than these indicated here.

2.2. Physico-chemical characterization of $LiFe_xTi_{2-x}O_4$

X-ray diffraction (XRD) patterns for phase identification were recorded on a Bruker D8 high-resolution X-ray powder diffractometer, equipped with a MBraun PSD-50 M detector, using monochromatic $CuK_{\alpha 1}$ radiation (λ = 1.5406 Å) obtained with a germanium primary monochromator. Data for structural refinements were collected in the angular range 2θ = 10–80º. Rietveld refinements were carried out by using the FULLPROF program suite [28]. Diffraction line profiles were approximated by pseudo-Voigt function. The refined instrumental and structural parameters were: zero shift, scale factor, background parameters, unit cell parameter, half width and mixing parameters U, V, W and η, asymmetry parameters, atomic positional parameters, individual isotropic displacement parameters, B_{iso}, and site occupancy factors (SOF).

In situ / *operando* XRD patterns were recorded on a Scintag V PAD diffractometer using CuKα1 (λ = 1.5406 Å) monochromatic radiation. A Swagelok-type electrochemical cell equipped with a beryllium window [29] was used for in situ/*operando* X-ray studies. Charge-discharge experiments were run at C/20 rate (1 Li ion inserted in 20 h) in the potential range 2–4.5 V vs. Li^+/Li using a MacPile galvanostat system. X-ray scans were recorded in the 15–50º 2θ range during a full electrochemical cycle.

Selected Area Electron Diffraction (SAED) and X-ray Energy Dispersive Spectroscopy (XEDS) were performed in a JEOL JEM 2000FX electron microscope, fitted with a double tilting goniometer (± 45°) and operating at 200 kV. EDS spectra were taken from several thin crystallites exhibiting electron diffraction patterns characteristics of the ramsdellite phases.

Surface morphology of ramsdellite materials was carried by means of SEM using a Thermo Fisher Scientific Prisma E instrument, equipped with an Everhart Thornley secondary electron Detector (ETD) at 25 kV and spot 2 (=19 pA). Elemental mapping was done by means of energy dispersive spectroscopy (EDS), using a backscattered electron detector (BSD) at 25 kV and spot 5 (= 1.3 nA).

Ramsdellite samples were further analyzed using the Spectrum Two Perkin Elmer Fourier Transform (FTIR) Spectrometer equipped with an Attenuated Total Reflectance (ATR) internal reflection system in the 4000–400 cm^{-1} wave number range. The resolution of the spectra was 4 cm^{-1}, and the data were collected in the transmittance mode.

Mössbauer spectra were recorded at room temperature with a conventional spectrometer equipped with a ^{57}Co(Rh) source. Energy calibration was made using an α-Fe (6 μm) foil. A non-linear fitting was made using the software NORMOS [30].

2.3. Electrochemical performance characterization

Galvanostatic cycling of $LiFe_xTi_{2-x}O_4$ was made on 8 mm-diameter pellets pressed from composite positive electrodes containing 85 wt% $LiFe_xTi_{2-x}O_4$ ramsdellite as active material, 10 wt% conductive carbon (Super C65) and 5 wt% PVDF as a binder. The mass load of active material was 12 mg in every electrode pellet. In all cases lithium metal disk was used as the negative electrode. The electrolyte was a 1 M solution of $LiPF_6$ in EC:DMC (1:1 vol%), and Whatman GF/D glass fibre was used as a separator. CR2032 coin cell assembly was performed in an argon-filled glove box (H_2O and O_2 content < 0.1 ppm). Galvanostatic cycling experiments were conducted in the low voltage range: ocv (open-circuit-voltage)1.0 V vs. Li^+/Li and in the high voltage range: ocv-4.5 V vs. Li^+/Li. Discharge-charge cycling was carried out at 25 ºC using the slow rate of C/30 (1 Li ion inserted in 30 h, 5.3 mA g^{-1}) and allowing for better comparison of the different samples closer to equilibrium condition. Longer cycling was carried out at the slow C/20 rate (1 Li ion inserted in 20 h, 8.0 mA g^{-1}) and the higher C/5 rate (1 Li ion inserted in 5 h, 31.8 mA g^{-1}). Power rate was further estimated for the x = 0.125 sample by determining the capacity at different current rates ranging from C/30–2 C (5.3 mA g^{-1} to 320 mA g^{-1}).

The slope of near-equilibrium voltage composition curve, ($\frac{dE}{dx}$), for different x were obtained from GITT (galvanostatic intermittent titration technique) data on charge. A cell was fully discharged down to 1 V at C/30 rate and equilibrated at such potential for 30 min. Cell was afterwards charged under GITT conditions (0.05 mA cm^{-2} for 30 min and relaxing until $|\Delta E/\Delta t| \langle$ 1 mV h^{-1} with a maximum relaxation time of 100 h).

Impedance spectroscopy measurements were carried out in the 10^6 Hz – 1 mHz frequency range applying a 10 mV AC perturbation. A VMP3 BioLogic battery tester equipped with an impedance channel was used. Impedance data analysis and equivalent circuit modelling were made by using ZView® software (Scribner Associates). To investigate the effect of aging on cell internal resistance impedance were measured on a fresh two-electrode cell and after it was cycled and subjected to increasing rates. However, to determine lithium diffusion coefficient and cathode contribution to internal resistance a three-electrode cell was used. It was cycled once under potentiostatic conditions and selected potentials were equilibrated during six hours to measure the variation of impedance with frequency as in a typical PEIS (potentiostatic electrochemical impedance spectroscopy) experiment. The low frequency range was used to determine the Warburg coefficient while cathode internal resistance due to cathode electrolyte interface and charge transfer were determined from the medium and high frequency range.

Specific area of the electrodes, taken as the better approach to the intercalation active area, was determined by nitrogen adsorption-desorption (BET method) using a Micromeritics ASAP 2420 analyzer.

3. Results and discussion

Powdered $LiFe_xTi_{2-x}O_4$ obtained from a mixture of Li_2CO_3, TiO_2, Fe_2O_3 and Ti_2O_3 yielded black products for x = 0, 0.125 with a slight dark-brownish tinge for x = 0.25, whereas products with higher iron content: x = 0.5, 0.75 and 1 were ocher to brick brown.

3.1. Structural characterization of the $LiFe_xTi_{2-x}O_4$ compounds

A general look at XRD patterns evidences a well-crystallized ramsdellite phase, indexed in Fig. 1, as unique or major phase for compositions $LiTi_2O_4$ (x = 0, Fig. 1a), $LiFe_{0.125}Ti_{1.875}O_4$ (x = 0.125, Fig. 1b), $LiFe_{0.25}Ti_{1.75}O_4$ (x = 0.25, Fig. 1c) and $LiFe_{0.5}Ti_{1.5}O_4$ (x = 0.5, Fig. 1d). However, despite the higher maximum synthesis temperatures used for the iron-rich compositions, 1275 ºC for x = 0.75 and 1400 ºC for x = 1, there was no evidence for a ramsdellite phase after quenching; composition $LiFe_{0.75}Ti_{1.25}O_4$ (x = 0.75, Fig. 1e) was indexed with a spinel major phase (labelled with SF) and pseudobrookite as minor secondary phase (labelled with PB) and $LiFeTiO_4$ (x = 1, Fig. 1f) was fully indexed with a spinel phase. Thus, an upper solubility limit of Fe_2O_3 in ramsdellite $LiTi_2O_4$ close to x = 0.5 can be inferred from XRD results. The observed higher stability of the spinel phase for iron-rich compounds is consistent with results from computational studies which predict much higher impractical temperatures well above the corresponding melting points, required to promote formation of the ramsdellite phase over the inverse spinel [25].

Selected area electron diffraction (SAED) patterns of samples with x = 0, 0.125, 0.25 and 0.5 were successfully indexed with an orthorhombic cell a ~ 5.0 Å, b ~ 9.6 Å, c ~ 2.9 Å. Fig. S1 exhibits typical ramsdellite patterns obtained in the [− 1 0 1] and [− 1 1 0] zone axes.

In general, Rietveld refinements started with a model in which both six-coordinated Fe and Ti fully occupied the same (4*c*) framework site with partial site occupancy factors (SOF) according to nominal composition, the (4*c*) tunnel site was half occupied by four-coordinated Li. The oxygen atoms fully occupied the (4*c*) site. In all cases, refinements of the starting model ended with acceptable values of statistical criteria for the fit, SOF and bond lengths. Main crystallographic parameters of all compositions are given in Table 1. Graphical results of Rietveld refinements of $LiFe_{0.125}Ti_{1.875}O_4$, $LiFe_{0.25}Ti_{1.75}O_4$ and $LiFe_{0.5}Ti_{1.5}O_4$ ramsdellites are gathered in Fig. S2a-c, together with their atomic positional and displacement parameters in Table S1a-c.

Table 1
Unit cell parameters versus composition for $LiFe_xTi_{2-x}O_4$ compounds as determined from X-ray powder diffraction ($0 \leq x \leq 1$).

x composition	a / Å	b / Å	c / Å	Vol / Å^3
0	5.0356(1)	9.6394(2)	2.9464(5)	143.02(1)[17]
	5.0356(6)	9.6477(8)	2.9484(7)	143.24(2)[22]
	5.0384(6)	9.6483(9)	2.9478(3)	143.30(3) This work
0.125	5.0225(1)	9.5969(2)	2.94771(6)	142.08(1)
0.25	5.0087(1)	9.6107(2)	2.94920(7)	141.97(1)
0.5	5.0164(5)	9.5592(8)	2.9482(2)	141.37(2)
0.75[a]	8.3618(5)	8.3618(5)	8.3618(5)	584.66(7)
1[b]	8.3657(5)	8.3657(5)	8.3657(5)	585.47(4)

[a] Unit cell parameters of the spinel major phase are given. Pseudobrookite as a minor secondary phase.
[b] Unit cell parameters of the spinel phase. Single-phase sample.

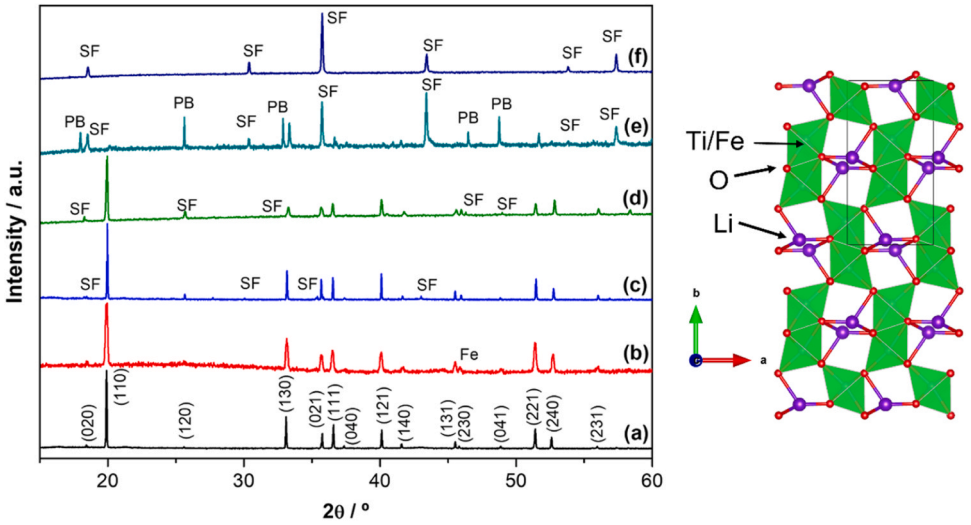

Fig. 1. X-ray diffraction patterns of $LiFe_xTi_{2-x}O_4$ ($0 \leq x \leq 1$) prepared at different final temperatures: (a) x = 0 at 1000 ºC; (b) x = 0.125 at 1010ºC; (c) x = 0.25 at 1250 ºC; (d) x = 0.50 at 1250 ºC; (e) x = 0.75 at 1275 ºC and (f) x = 1.0 at 1400 ºC. PB = pseudobrookite; SF = face-centered spinel; Fe = iron. Representation of the ramsdellite structure with space group *Pbnm*. $(Ti/Fe)O_6$ octahedra (green), lithium (purple spheres) and oxygen (red spheres).

The XRD pattern of undoped $LiTi_2O_4$ (Fig. 1a) was indexed with the primitive orthorhombic lattice of ramsdellite, space group *Pbnm* and unit cell parameters a = 5.0384(6) Å, b = 9.6483(9) Å, c = 2.9478(3) Å, in excellent agreement with previous reports [8,26,31].

XRD phase analysis of $LiFe_{0.125}Ti_{1.875}O_4$ (Fig. 1b) showed *Pbnm* ramsdellite major phase with unit cell parameters a = 5.0225(1) Å, b = 9.5969(2) Å, c = 2.94771(6) Å, accompanied by a ~2.2 wt% of elemental α-iron (space group *Im*-3*m*, a = 2.8667(4) Å) as deduced from quantitative phase analysis using the Rietveld method. Attempts for eliminating this minor impurity by additional heating failed. The presence of iron as minor secondary phase is explained by reaction of some iron(III) oxide with titanium(III) oxide used as reactant in the synthesis of ramsdellite:

$$3\ Ti^{3+} + Fe^{3+} = 3\ Ti^{4+} + Fe^{0} \quad (2)$$

On the other hand, the proposed Ti^{3+} driven reductive mechanism is associated with a lower iron content in the ramsdellite phase and segregation of some metallic iron, no longer available for the ramsdellite phase. Consistent with this, XEDS performed on individual crystals exhibiting diffraction patterns characteristic of ramsdellite always shows some iron understoichiometry, and the observed composition corresponds to $LiFe_{0.078}Ti_{1.875}O_4$ (Table 2). In refinements, a lower site occupancy of iron on the octahedral (4*c*) site reduced the residual R_{wp} value significantly, further supporting the octahedral metal vacancy model, i.e. $(Li)_c\ (Fe_{0.078}\square_{0.047}Ti_{1.875})_f\ O_4$ (□ = vacancies, *c* = channel, *f* = framework). The difference between nominal atoms of iron (0.125) and experimental atoms of iron (0.078) per formula unit deduced from XEDS, 0.047, is tantamount to a 1.6 wt% of iron, in very good agreement with XRD results.

XRD phase analysis of $LiFe_{0.25}Ti_{1.75}O_4$ (Fig. 1c) confirmed ramsdellite major phase with unit cell parameters a = 5.0087(1) Å, b = 9.6107 (2) Å, c = 2.94920(7) Å. In refinements, relative site occupancies of iron and titanium on the octahedral (4*c*) site remained stable and close to nominal compositions, in agreement with results from XEDS (Table 2). Quantitative phase analysis using the Rietveld method yielded a ~8 wt % of a face-centered cubic spinel phase, space group *Fm*-3*m*, as secondary minor phase. The observed unit cell parameter of spinel, a = 8.4041(4) Å), goes beyond the range 8.33 < a < 8.36 Å, reported for several Fe^{3+} containing ordered spinels $Li_{(1+x)/2}Fe_{(5-3x)/2}Ti_xO_4$ ($0 \le x \le 0.4$) and ($1.28 \le x \le 1.56$) [32]. This could be an indication for the presence of Fe^{2+} in the spinel phase [27]. However, presence of Ti^{3+} may also explain an increased unit cell parameter, from 8.35 Å to 8.40 Å as observed in spinels $Li_{1+x}(Ti^{3+}_{1-3x}Ti^{4+}_{1+2x})O_4$ ($0 \le x \le 1/3$) [33]. Following the structural section, results from ^{57}Fe Mössbauer spectroscopy will be used to provide a more detailed understanding of the oxidation states of iron.

Main reflections of the XRD pattern displayed by $LiFe_{0.5}Ti_{1.5}O_4$ (Fig. 1d) were indexed with a ramsdellite major phase and unit cell parameters a = 5.0164(5) Å, b = 9.5592(8) Å, c = 2.9482(2) Å. Relative site occupancies of iron and titanium on the octahedral (4*c*) site remained stable and close to nominal compositions, which is consistent with XEDS (Table 2). Quantitative phase analysis using the Rietveld method yielded a ~9 wt% of a cubic spinel phase as secondary minor phase. Alike $LiFe_{0.25}Ti_{1.75}O_4$, the observed unit cell parameter of spinel, a = 8.386(3) Å) is beyond the range 8.33 < a < 8.36 Å reported for Fe^{3+} and Ti^{4+} containing spinels, indicative for the presence of either Fe^{2+}, Ti^{3+} or both cations in this minor phase. Because of the low relative contribution of this phase in XRD patterns it cannot undoubtedly be ascertained if the spinel adopts the face-centered cubic *Fm*-3*m* or the primitive cubic $P4_332$ space group reported for spinel $LiFe_{0.5}Ti_{1.5}O_4$ [27].

Table 2
Nominal compositions and estimated from XEDS for ramsdellites $LiTi_{2-x}Fe_xO_4$.

x in $LiFe_xTi_{2-x}O_4$	Nominal composition	Estimated composition
0.125	$LiFe_{0.125}Ti_{1.875}O_4$	$LiFe_{0.07(1)}Ti_{1.87(1)}O_4$
0.25	$LiFe_{0.25}Ti_{1.75}O_4$	$LiFe_{0.24(1)}Ti_{1.76(1)}O_4$
0.5	$LiFe_{0.5}Ti_{1.5}O_4$	$LiFe_{0.46(1)}Ti_{1.54(1)}O_4$

Fig. 2 shows the variation of lattice parameters and unit cell volume for ramsdellites $LiFe_xTi_{2-x}O_4$ with x = 0, 0.125, 0.25 and 0.5, as a function of the nominal iron composition, x. Taking into account Shannon ionic radii for high spin Fe^{3+}(VI) = 0.645 Å and Ti^{3+}(VI) = 0.67 Å [34], a slight but continuous decrease of lattice parameters and unit cell volume would be expected for an isovalent Ti^{3+}-Fe^{3+} substitution. It has been shown that in $Li_{1-x}Ti_2O_4$ [35] and $Li_{1+x}Ti_{2-2x}O_4$ [36] ramsdellites, the *b* axis, which relates to the longer cross-channel direction, is clearly the most sensitive to extent of substitution of Ti^{3+} by Ti^{4+} and decreases with increasing oxidation state of titanium. The *a* unit-cell edge also decreases as Ti oxidation state increases; however, *c*, which is parallel to the channels, is essentially invariant with composition. And although the situation in iron-substituted ramsdellites appears more complex with two active redox couples, Ti^{4+}/Ti^{3+} and Fe^{3+}/Fe^{2+}, a general shortening of the lattice parameters *a* and *b* as well as the unit cell volume indicates transition to a higher oxidation state of iron, titanium or both species. This trend is clearly fulfilled for compositions x = 0.125 and 0.5. On the other hand, composition x = 0.25 presents the expected tendency in *a* parameter, while *b* parameter shows an opposite trend, pointing to a more complex substitution mechanism, most likely related to a slightly different situation of oxidation states of iron and titanium.

IR spectra of $LiFe_xTi_{2-x}O_4$ ramsdellites are shown in Fig. S3. Strong IR bands below 800 cm^{-1} in all compositions are characteristic of the M-O (M=Fe,Ti) ramsdellite framework. The bands in the region 1600–1400 cm^{-1} are ascribed to M-O-M vibrational modes [37–40]. The absence of other vibrational modes in the 3400–3200 cm^{-1} and 1700–1600 cm^{-1} range confirms the absence of hydroxyl M-OH or structural water in these compounds [37–40], which were obtained by the high temperature synthetic route.

3.2. Elemental and surface morphological characterization of $LiFe_xTi_{2-x}O_4$ ramsdellites

The morphology of $LiFe_xTi_{2-x}O_4$ ramsdellites was analyzed by SEM and is shown in Fig. 3. In general, average particle sizes were in the micrometer range exhibiting well crystallized prismatic shape. However, significant differences in particle size exist for ramsdellites with low and high Fe-doping, which is attributed to the different synthesis temperatures employed. As described in the experimental section, $LiTi_2O_4$ and the low Fe-doped $LiFe_{0.125}Ti_{1.875}O_4$ ramsdellites synthesized at lower temperatures (1000–1010 °C) produce smaller particles in the 5–8 μm range, whilst the higher temperatures (1250–1275 °C) required to synthesize higher Fe-doped ramsdellites $LiFe_{0.25}Ti_{1.75}O_4$ and $LiFe_{0.5}Ti_{1.5}O_4$ lead to larger particles in the 10–50 μm range. The SEM-EDX mapping shown in Fig. 3 demonstrates the uniform distribution of Ti, O in all ramsdellites. As expected, Fe content increases with increasing Fe-doping in ramsdellites (upper row, left-to-right in Fig. 3), evident from an increasing intensity of the green false color. It is worth mentioning that the isolated green spots in sample $LiFe_{0.125}Ti_{1.875}O_4$ are ascribed to metallic iron, already detected by X-ray diffraction, due to the absence of both Ti and O (visible as white spots) for the same objects.

3.3. Oxidation state of iron in $LiFe_xTi_{2-x}O_4$ ramsdellite phases

^{57}Fe Mössbauer spectra were recorded for Fe-substituted $LiFe_xTi_{2-x}O_4$ ramsdellites with compositions x = 0.125, 0.25 and 0.5 aimed at unraveling oxidation state and coordination of iron. The spectral parameters: isomer shift (IS), quadrupole splitting (QS), relative contribution of the subspectra (A) to the spectrum and attribution derived from fits are presented in Table 3.

As seen from Fig. 4a, the spectrum of sample $LiFe_{0.125}Ti_{1.875}O_4$ (x = 0.125) is fitted with two quadrupole doublets corresponding to iron

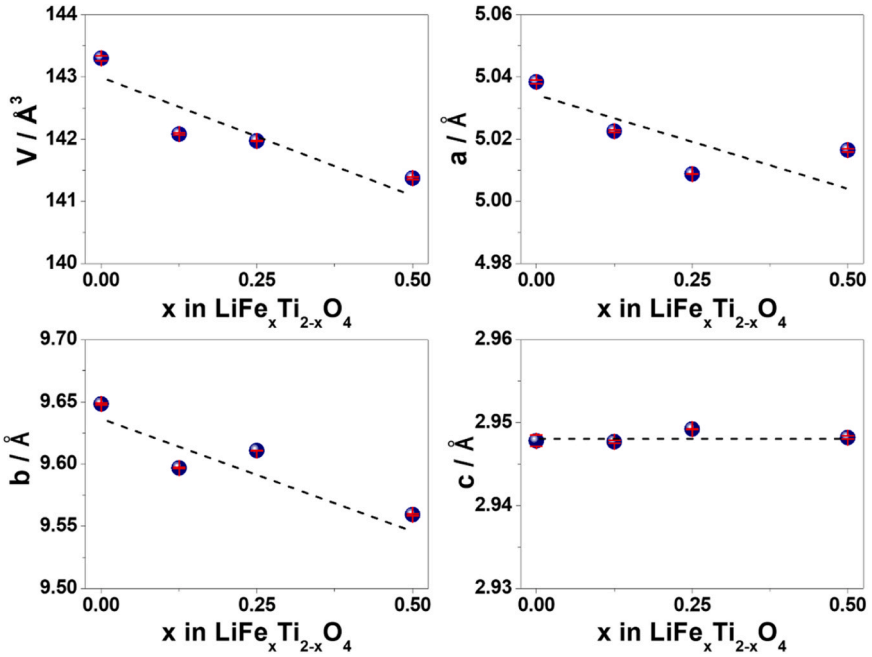

Fig. 2. Variation of lattice parameters and unit cell volume for $LiFe_xTi_{2-x}O_4$ ramsdellites (x = 0, 0.125, 0.25 and 0.5) as a function of iron composition, y. For x = 0 reference data from Gover et al. [26] and Akimoto et al. [31] have been included. The dotted lines provide guides to the eye.

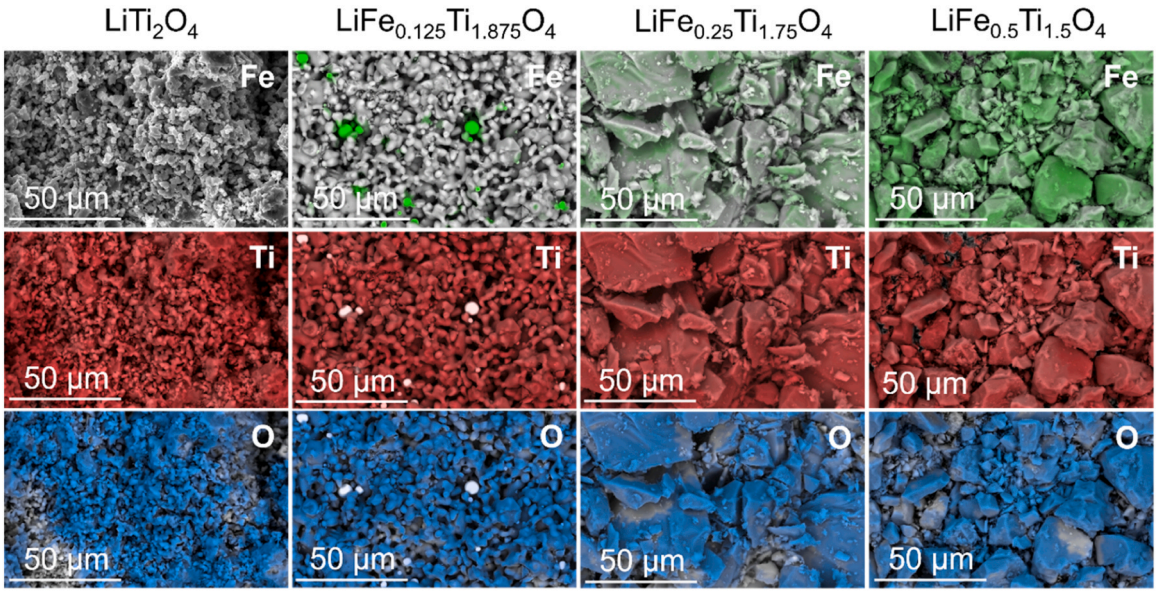

Fig. 3. SEM images of ramsdellites (from left-to-right): $LiTi_2O_4$, $LiFe_{0.125}Ti_{1.875}O_4$, $LiFe_{0.25}Ti_{1.75}O_4$ and $LiFe_{0.5}Ti_{1.5}O_4$ with the corresponding elemental mapping.

atoms located in octahedral sites with oxidation states Fe^{3+} (IS = 0.36 mm/s, QS = 0.65 mm/s) and Fe^{2+} (IS = 0.98 mm/s, QS = 2.29 mm/s), both associated with the ramsdellite phase. Values of IS and QS for both octahedral Fe^{3+} and Fe^{2+} are in agreement with those reported for Fe-doped $Li_2Ti_3O_7$ ramsdellite [41]. However, the spectrum is more complex since the two quadrupole doublets are overlapped with a sextet corresponding to an important segregation of α-Fe(0) (IS ~0.00 mm/s, QS ~0.00 mm/s), detected by XRD. In addition, a sextet ascribed to Fe_3C, not observed in XRD, was also present. The relative contributions of ramsdellite and α-Fe to the spectrum are in good agreement with results from quantitative XRD phase analysis. The relatively lower contribution of iron carbide or nitride, corresponding to < 1% by weight, makes it undetectable by XRD. The presence of Fe^{2+} (43.8% of iron in ramsdellite) is explained by reaction of iron(III) oxide with titanium(III) oxide in the synthesis of ramsdellite:

$$Ti^{3+} + Fe^{3+} = Fe^{2+} + Ti^{4+} \quad (3)$$

Bearing in mind results from XRD, XEDS and Mössbauer, the following composition for nominal $LiFe_{0.125}Ti_{1.875}O_4$, i.e. $LiFe^{3+}_{0.125}Ti^{3+}_{0.875}Ti^{4+}O_4$, is proposed, considering reductive segregation of Fe (0), Eq. 2, and formation of Fe^{2+}, Eq. 3: $LiFe^{3+}_{0.078}Ti^{3+}_{0.734}Ti^{4+}_{1.141}O_4$ (after Eq. 2) and $LiFe^{2+}_{0.034}Fe^{3+}_{0.044}Ti^{3+}_{0.700}Ti^{4+}_{1.175}O_4$ (after Eq. 3).

The spectrum of the sample with nominal composition $LiTi_{1.75}Fe_{0.25}O_4$ (x = 0.25, Fig. 4b) can be interpreted as the sum of three quadrupolar doublets with hyperfine parameters shown in Table 3. Two doublets were ascribed to iron atoms located in octahedral sites with oxidation states Fe^{3+} (IS = 0.36 mm/s, QS = 0.47 mm/s) and Fe^{2+} (IS =

Table 3
^{57}Fe Mössbauer spectral parameters for ramsdellite samples with nominal composition $LiTi_{1.875}Fe_{0.125}O_4$, $LiTi_{1.75}Fe_{0.25}O_4$, and $LiTi_{1.5}Fe_{0.5}O_4$ at room temperature.

Sample	IS[a] (mm/s)	QS (mm/s)	H (T)	A %	Attribution
$LiTi_{1.875}Fe_{0.125}O_4$	0.36(2)	0.65(4)	-	9(1)	$(Fe^{3+})_O$ R
	0.98(2)	2.29(4)	-	7(1)	$(Fe^{2+})_O$ R
	0.21(2)	0.04(4)	20.5(1)	17(1)	Fe_3C
	0.001(1)	0.001(2)	32.8(1)	67(1)	α-Fe
$LiTi_{1.75}Fe_{0.25}O_4$	0.366(1)	0.475(4)	-	77(1)	$(Fe^{3+})_O$ R
	0.98(2)	2.46(2)	-	8(1)	$(Fe^{2+})_O$ R
	0.272(6)	0.86(1)	-	15(1)	$(Fe^{3+})_O$ S
$LiTi_{1.5}Fe_{0.5}O_4$	0.367(3)	0.480(7)	-	67(1)	$(Fe^{3+})_O$ R
	0.970(6)	2.33(1)	-	13(1)	$(Fe^{2+})_O$ R
	0.94(2)	0.77(4)	-	20(1)	$(Fe^{2+})_T$ S

[a] IS relative to α-Fe center shift.

0.98 mm/s, QS = 2.46 mm/s), both associated with the ramsdellite phase. Again, values of IS and QS for both octahedral Fe^{3+} and Fe^{2+} are in agreement with those reported for Fe-doped $Li_2Ti_3O_7$ ramsdellite and similar to those observed in composition x = 0.125.

The relative fraction of the two ramsdellite spectral components accounts for 85% of total Fe (77% Fe^{3+}, 8% Fe^{2+}), which allows reformulation of nominal $LiFe^{3+}_{0.25}Ti^{3+}_{0.75}Ti^{4+}O_4$, considering reductive formation of Fe^{2+} according to Eq. 3, to composition $LiFe^{2+}_{0.02}Fe^{3+}_{0.23}Ti^{3+}_{0.73}Ti^{4+}_{1.02}O_4$. The third doublet is associated with iron atoms located in octahedral sites and oxidation state Fe^{3+} (IS = 0.27 mm/s, QS = 0.86 mm/s) of the spinel minor phase observed by XRD. IS and QS values are in the range for octahedral Fe^{3+} previously reported in Fe-doped $Li_4Ti_5O_{12}$ [41] and $LiTi_{1.9}Ca_{0.1}(PO_4)_3$ [42]. Considering the weight fraction of the spinel phase determined from XRD (8 wt%), the higher relative fraction of this spectral component (15 at% Fe) suggests a higher iron content for the spinel phase, corresponding to a composition $LiFe_{0.48}Ti_{1.52}O_4$, i.e. $LiFe^{3+}_{0.48}Ti^{3+}_{0.52}Ti^{4+}O_4$. Since Fe^{2+} is ruled out in the present spinel phase, the similarity in lattice parameter (a = 8.404 Å) with previously reported $LiFe^{2+}_{0.5}Ti^{4+}_{1.5}O_4$ [33] is ascribed to the presence of Ti^{3+}, which also explains an increased lattice parameter compared to $LiFe^{3+}Ti^{4+}O_4$ (a=8.362 Å), in agreement with Shannon ionic radii for Ti^{3+}(VI) = 0.67 Å and Ti^{4+}(VI) = 0.605 Å.

The spectrum of the sample $LiTi_{1.5}Fe_{0.5}O_4$ (x = 0.5) as seen from Fig. 4c is fit with three quadrupole doublets, and characteristic Mössbauer parameters together with the assignation of the three detected species are shown in Table 3. Two doublets were ascribed to iron atoms located in octahedral sites of the ramsdellite structure, centered at 0.36 mm/s and 0.97 mm/s indicative for Fe^{3+} and Fe^{2+} oxidation states, respectively. QS for octahedral Fe^{3+} (0.48 mm/s) and Fe^{2+} (2.33 mm/s) were comparable to those observed in compositions x = 0.125 and 0.25. Both octahedral sub-spectra associated with the ramsdellite phase account for 80% of total Fe (67% Fe^{3+}, 13% Fe^{2+}), which allows to reformulate nominal $LiFe^{3+}_{0.50}Ti^{3+}_{0.50}Ti^{4+}O_4$, considering reductive formation of Fe^{2+} according to Eq. 3, to the composition $LiFe^{2+}_{0.08}Fe^{3+}_{0.42}Ti^{3+}_{0.42}Ti^{4+}_{1.08}O_4$. IS of the third doublet (0.94 mm/s) is indicative for Fe^{2+} associated with iron atoms located in tetrahedral (8*a*) sites of the spinel minor phase observed by XRD with a smaller QS of 0.77 mm/s. Taking into account the weight fraction of the spinel phase determined from XRD (10 wt%), the higher relative fraction of this spectral component (20 at% Fe) suggests a higher iron content for the spinel phase. Since all Fe^{2+} is associated with the tetrahedral 8*c* site in an inverse spinel structure, a reductive formation of Fe^{2+} in spinel $LiFe^{3+}_{0.5}Ti^{3+}_{0.5}Ti^{4+}O_4$ according to Eq. 3 combined with the following substitution mechanism in Eq. 4 is proposed:

$$(Ti^{4+})_f + (2\ Li^+)_c = (3\ Fe^{2+})_c \quad (4)$$

yielding the general composition $Li_{1-2x}Fe^{2+}_{0.5+3x}Ti^{4+}_{1.5-x}O_4$. For x = 1/6, four-coordinated Fe occupies the 8*c* site in composition $(Fe^{2+})_t(Li^+_{0.67}Ti^{4+}_{1.33})O_4$, matching both observed at% (Mössbauer) and wt % (XRD) Fe for the spinel phase.

3.4. Electrochemical study of $LiFe_xTi_{2-x}O_4$ ramsdellites

3.4.1. Low voltage range. Discharge from ocv to 1 V

Fig. 5 shows the discharge-charge profiles of the four ramsdellite samples (x = 0, 0.125, 0.25 and 0.5) down to 1 V at a 5.3 mA g^{-1} constant current density equivalent to a C/30 rate. The first discharge capacities are 118 mAh g^{-1} (x = 0), 179 mAh g^{-1} (x = 0.125), 137 mAh g^{-1} (x = 0.25) and 135 mAh g^{-1} (x = 0.5). In addition, the progressive

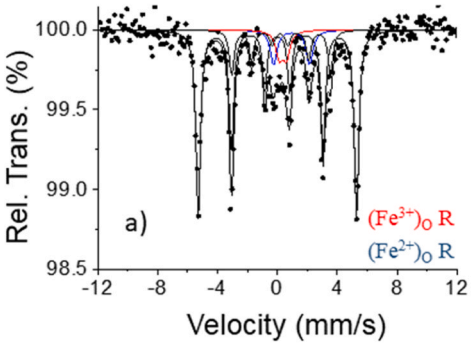

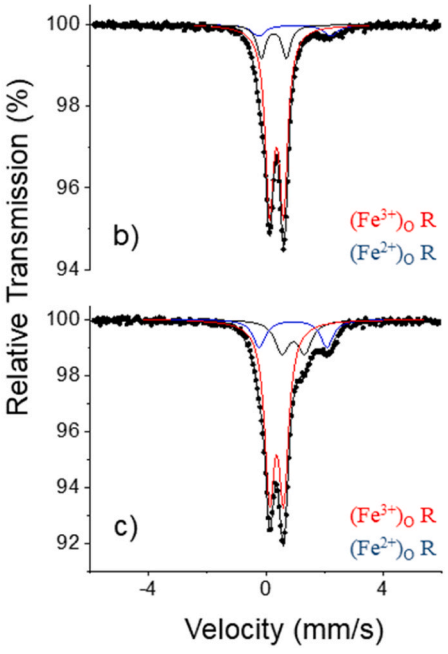

Fig. 4. ^{57}Fe Mössbauer spectra of ramsdellites: a) $LiFe_{0.125}Ti_{1.875}O_4$, b) $LiFe_{0.25}Ti_{1.75}O_4$ and c) $LiFe_{0.5}Ti_{1.5}O_4$ at room temperature. Red line: $(Fe^{3+})_O$, blue line: $(Fe^{2+})_O$.

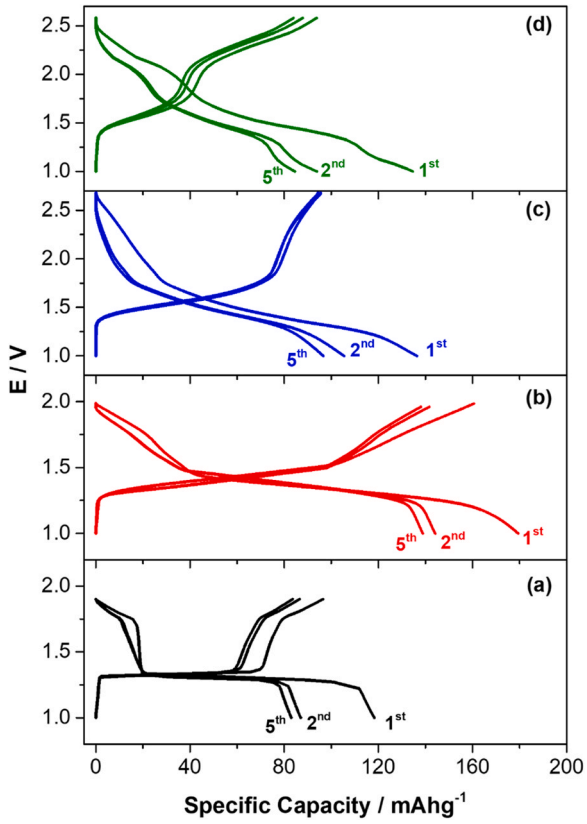

Fig. 5. Discharge-charge capacities for 1st, 2nd and 5th cycle of ramsdellites $LiFe_xTi_{2-x}O_4$ with x = 0 (a), x = 0.125 (b), x = 0.25 (c) and x = 0.5 (d). All cells were cycled at C/30.

Fe substitution is accompanied by an increase in the *ocv* rest potential, from ca. 1.8 V vs. Li^+/Li in x = 0 to 2.65 V vs. Li^+/Li in x = 0.5. For x = 0 and x = 0.125, two "S"-shaped profiles at the beginning and the end of discharge enclose a plateau (a quasi-constant voltage region) developed at 1.3–1.4 V. This characteristic has been previously interpreted in ramsdellite $LiTi_2O_4$ as a two-phase domain sandwiched by solid solutions at both ends of the biphasic region [19]. For compositions x = 0.25 and x = 0.5, discharge curves exhibit an "S"-shape profile, which may indicate a single-phase insertion mechanism for lithium throughout the whole discharge process. On the other hand, increasing internal resistance due to progressive Fe substitution, in combination with increasing cell polarization, may also lead to a less horizontal, more curved voltage profile, as it has been demonstrated for V-substituted $LiTi_2O_4$ ramsdellites [22]. A closer look at the discharge profile reveals an emerging second electrochemical process at a potential > 2 V with increasing iron content, which is clearly visible for x = 0.50 (Fig. 4c) and also developed upon charge. Considering its absence in the undoped sample (x = 0), this process is hence ascribed to the reversible redox behavior of the $Fe^{3+/2+}$ redox pair. Worth mentioning that the reduction of Fe^{3+} in other Fe-substituted ramsdellites ($Li_2Ti_3O_7$) or in the compositionally related spinel $Li_{1+x}Fe_{1-3x}Ti_{1+2x}O_4$ [43,44] is not reversible. From discharge-charge profile, the amount of electrochemically active Fe^{3+} involved in the electrochemical lithium insertion-deinsertion during the first discharge-charge cycle was estimated to be 0.10 Fe/f.u. for x = 0.25 and 0.25 Fe/f.u. for x = 0.50, suggesting that not all Fe^{3+} is actively involved (theoretically 0.23 Fe^{3+}/f.u. for x = 0.25 and 0.42 Fe^{3+}/f.u. for x = 0.50). In this sense, capacities developed below 1.75 V, ascribed to the reversible $Ti^{4+/3+}$ redox pair, are also systematically lower than the amount of Ti^{4+} present in the ramsdellite: x = 0 (0.75 vs. 1 Ti^{4+}), x = 0.125 (1.0 vs. 1.175 Ti^{4+}) x = 0.25 (0.65 vs. 1.02 Ti^{4+}), and x = 0.50 (0.60 vs. 1.08 Ti^{4+}). It turns out that ramsdellite $LiFe_{0.125}Ti_{1.875}O_4$ (x = 0.125) exhibits the highest percentage of active Ti^{4+} (89%) among the studied ramsdellites.

Table 4 compares experimental first discharge and reversible capacities with theoretical capacities of $LiFe_xTi_{2-x}O_4$ ramsdellites. Two values of theoretical capacities are given. One is based on 1 Li^+/formula unit (f.u.), reported by other authors as the maximum amount of insertable lithium into the tunnel space of the ramsdellite structure. The second one considers the amount of all reducible metal ions, i.e. the sum of Fe^{3+} and Ti^{4+} available in the ramsdellite structure as deduced from X-ray diffraction and Mössbauer spectroscopy. Remarkably, the ramsdellite $LiFe_{0.125}Ti_{1.875}O_4$ (x = 0.125) shows the best electrochemical behavior; its discharge capacity exceeds the theoretical 1 Li^+/f.u. in the first discharge and is withstood in the following cycles close to the theoretical capacity. Moreover, the irreversible capacity loss is significantly lower (18%) when compared to ramsdellites with higher iron content, x = 0.25 (23%) and x = 0.50 (30%).

The better cycling properties of ramsdellites $LiFe_{0.125}Ti_{1.875}O_4$ (x = 0.125) are clearly observed in Fig. 6, which compares cycle stability and Coulombic efficiency at the low current rate of C/20 (upper row of Fig. 6) and the higher current of C/5 (lower row of Fig. 6) for the ramsdellite series x = 0, 0.125, 0.25, 0.5 (Fig. 6a-d). In all ramsdellites, Coulombic efficiencies achieve values close to 100% after the first five cycles.

Further prove of the outstanding electrochemical properties of $LiFe_{0.125}Ti_{1.875}O_4$ is given in Fig. 7 which compares the capacity retention of $LiFe_{0.125}Ti_{1.875}O_4$ with that of undoped $LiTi_2O_4$ ramsdellite at increasing C rates (Fig. 7a) and upon longer cycling at the higher C/5 current rate (Fig. 7b). Two active redox pairs, $Ti^{4+/3+}$ and $Fe^{3+/2+}$, combined with a higher amount of available active Ti^{4+} and better electrical properties due to the presence of metallic iron, boosting farther electronic conductivity in $LiFe_{0.125}Ti_{1.875}O_4$, allow the remarkable capacity of 179 mAh g^{-1} at the low C/30 (5.3 mA g^{-1}), whilst a noticeable capacity of 71 mAh g^{-1} is still held at the high current of 2 C (320 mA g^{-1}) (Fig. 7a). In line with this, the discharge capacity of $LiFe_{0.125}Ti_{1.875}O_4$ at higher C/5 (Fig. 7b) after cycle 2 (125 mAh g^{-1}) and cycle 60 (120 mAh g-1) are impressively higher compared with undoped $LiTi_2O_4$ at identical current (75 mAh g^{-1} after cycle 2, 70 mAh g^{-1} after cycle 60).

Table 5 shows a summary with selected TiO_2-based ramsdellite electrodes reported in literature and in this work for LIBs showing remarkable electrochemical properties.

The cell bearing $LiFe_{0.125}Ti_{1.875}O_4$ as the active material of the positive electrode was investigated by impedance spectroscopy. A typical Nyquist plot of the impedance data of the two-electrode cell at open circuit voltage but subjected at 10 mV *ac* perturbation inducing a

Table 4
Theoretical and experimental discharge capacity at C/30 rate of $LiFe_xTi_{2-x}O_4$ ramsdellites.

Nominal x in $LiFe_xTi_{2-x}O_4$	Theoretical capacity (mAh g^{-1}) (1 Li^+/f.u.)	Theoretical capacity (mAh g^{-1}) (Fe^{3+}+Ti^{4+})	1st cycle discharge capacity (mAh g^{-1})	2nd cycle capacity (mAh g^{-1})
0	161	161	113[13] 118 (this work)	- 84
0.125	162	198	179	146
0.25	159	199	137	105
0.5	157	236	135	94

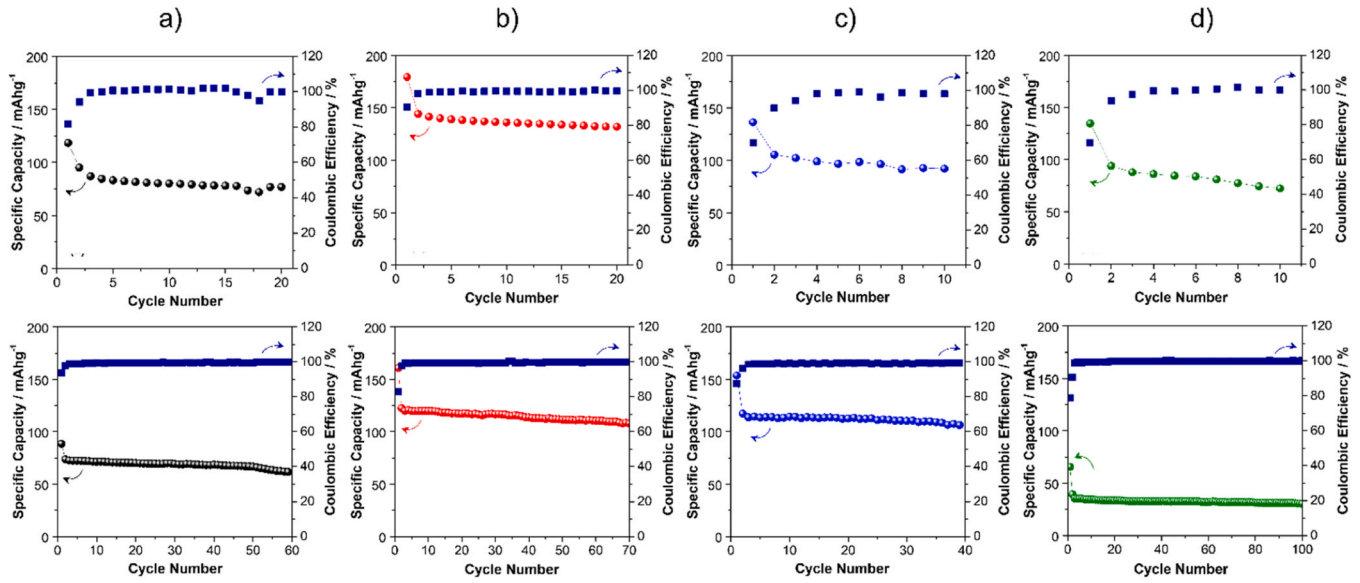

Fig. 6. Evolution of specific capacity and Coulombic efficiencies with cycle number at the low C/20 (upper row) and the higher C/5 current rate (lower row) for ramsdellites $LiFe_xTi_{2-x}O_4$ with x = 0 (a), x = 0.125 (b), x = 0.25 (c) and x = 0.50 (d).

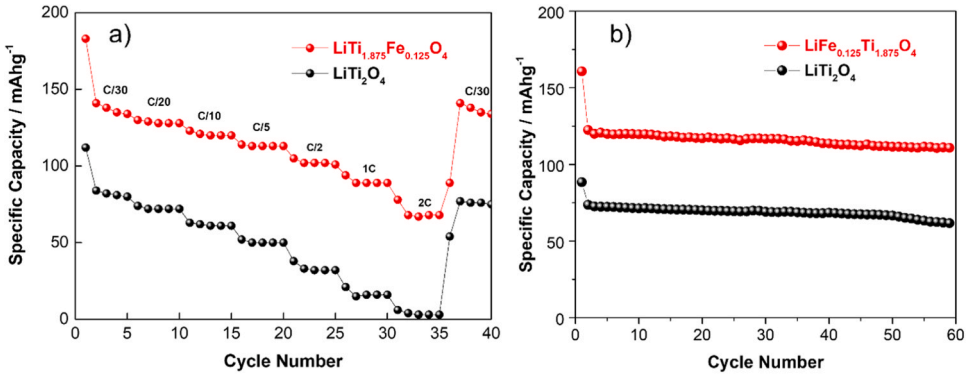

Fig. 7. Rate capability at various rates ranging from low C/30 to high 2 C (a) and discharge-charge cycling at C/5 (b) of ramsdellites $LiTi_2O_4$ (black dots) and $LiFe_{0.125}Ti_{1.875}O_4$ (red dots).

Table 5
Electrochemical performance of selected TiO_2-based ramsdellites as anode materials for Li-ion batteries.

Compound	Electrolyte	Cycle performance (mAh g^{-1}/mA g^{-1})	Rate performance (mAh g^{-1}/mA g^{-1})	Potential (V)	Reference
TiO_2	1 M $LiClO_4$ in EC:DEC (1:1)	190 (60th)/-		0.0–3.0[a]	[20]
	1 M $LiPF_6$ in EC:DMC (1:1)	241 (12th)/-		0.8–2.8[a]	[9]
CNT-TiO_2	1 M $LiPF_6$ in EC:DMC (1:1)	230 (50th)/26.8	280/5.4	1.2–3.0[a]	[21]
			100/1608	1.2–3.0[a]	
$Li_{0.47}TiO_2$	1 M $LiPF_6$ in EC:DEC (1:1)	200 (4th)/130	208/130	0.8–3.0[a]	[45]
			160/649	0.8–3.0[a]	
V-doped TiO_2	1 M $LiPF_6$ in EC:DMC (1:1)	250 (20th)/-		1.0–4.2[a]	[24]
$LiTi_2O_4$	1 M $LiClO_4$ in EC:DEC (1:1)	113 (1st)/-		1.3–2.0	[20]
		75 (20th)/5.4	75/8.0	1.0–2.0	This work
	1 M $LiPF_6$ in EC:DMC (1:1)	70 (60th) 32.1	10/161	1.0–2.0	
$LiTiVO_4$	1 M $LiPF_6$ in EC:DMC (1:1)	155 (1st)/-		1.0–2.8	[22]
$LiCrTiO_4$	1 M $LiPF_6$ in EC:DMC (1:1)	95(15th)/-		1.0–3.5	[23]
$LiFe_{0.125}Ti_{1.875}O_4$	1 M $LiPF_6$ in EC:DMC (1:1)	175 (20th)/8.0	130/8.0	1.0–2.0	This work
		115 (70th)/32.1	72/332	1.0–2.0	
$LiFe_{0.25}Ti_{1.75}O_4$	1 M $LiPF_6$ in EC:DMC (1:1)	100 (10th)/8.0		1.0–2.8	This work
		95 (40th)/32.1		1.0–2.8	
$LiFe_{0.50}Ti_{1.50}O_4$	1 M $LiPF_6$ in EC:DMC (1:1)	75 (10th)/8.0		1.0–2.7	This work
		28 (100th)/32.1		1.0–2.7	

[a] Ramsdellite electrodes were studied in the wide potential range. At most half of the here stated capacity corresponding to the low potential range would be suitable for practical application as anode material in LIBs.

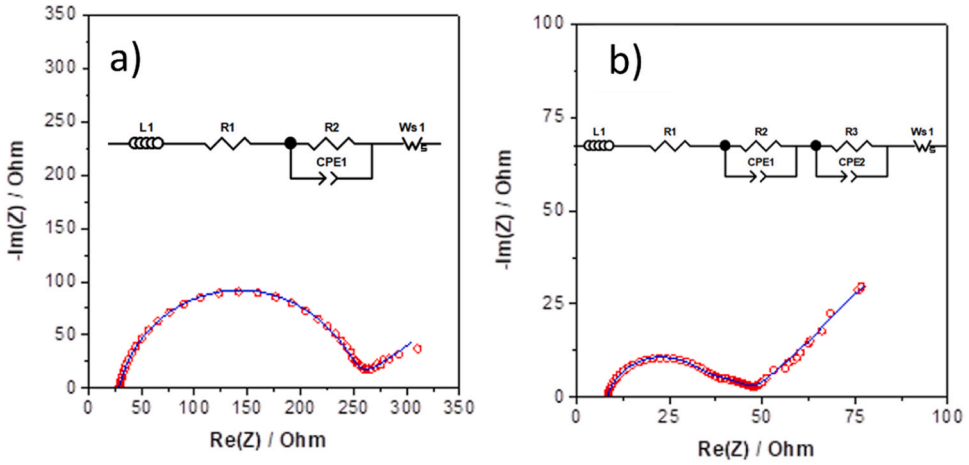

Fig. 8. Nyquist plots corresponding to the impedance of two-electrode cells $LiFe_{0.125}Ti_{1.875}O_4$ (composite 85:10:5)// Li; a) fresh cell and b) cycled cell (40 cycles at different rate). The experimental data are shown as red circles while the solid blue line depicts the fitting to the equivalent circuit shown in the inset.

lithium intercalation/deintercalation of a small amount of lithium (dilute conditions) is shown in Fig. 8a. The corresponding plot after cycling at C/20 (as in Fig. 6) is shown in Fig. 8b. The equivalent circuits used to model the impedance response in each case are shown in the corresponding insets. Capacitors have been replaced by constant phase elements (CPE) to account for the inhomogeneities and roughness of surfaces. For the cycled cell it consists in an inductance (L1) arising from cell components. R_1 is used to take into account the fast migration (high frequency) of lithium through the electrolyte and separator. Two semicircles can be seen at intermediate frequency. The one at higher frequency is modelled with a R_2CPE_1 element that may be due to the resistance and capacitance of interfaces (Rint and CPEint), while the one at lower frequency, modelled with R_3CPE_2 element may correspond to charge transfer resistance and capacitance of electrical double layer (R_{CT} and CPE_{EDL}). Because the Fe-substituted ramsdellite is electronically conductive (high content of Ti^{3+}) the ascription of this semicircle to bulk electronic resistance and polarizability of ramsdellite has not been considered. It follows an inclined sloping line at low frequency which corresponds to mass diffusion. Despite the slight dispersion of experimental data, it can be seen that it follows a straight line with slope= 1 and thus, it has been modelled with a Warburg resistance (W_s) with a 0.48 exponent (ideally 0.5 when semi-infinite linear diffusion, SILD, occurs). On the other hand, for the fresh cell a modified circuit was used, inasmuch as only one semicircle is clearly seen, and a higher dispersion of experimental data was observed at low frequencies that was not included in the modelling. Fitting to the two contributions (interfaces and charge transfer) would be in this case highly dependent on the starting values. Thus, individual components have not been determined. However, relevant information can be extracted. The resistance of the fresh cell due to electrolyte, interfaces and charge transfer is very much reduced (from 257 to 47 ohms) upon cycling. $LiFe_{0.125}Ti_{1.875}O_4$ is therefore a low impedance electrode sustaining its high capacity at high rate as it is shown in Fig. 7a. Data also indicate that it forms a very stable cathode electrolyte interface and electrolyte is not consumed.

Visible spikes corresponding to mass diffusion are observed in Fig. 8. However, it cannot be used for determination of lithium diffusion coefficient of $LiFe_{0.125}Ti_{1.875}O_4$ because the contribution of the anode may be also significant in the low frequency range. Thus, a three-electrode cell was run using metallic lithium disks as counter and reference electrode, respectively. By doing so it is confirmed that impedance of lithium in the low frequency range is only one order of magnitude lower than the working electrode. Therefore, lithium diffusion coefficient had to be determined using a three-electrode cell to avoid counter electrode contribution. The 3-electrode cell with the positive electrode made of a composite pellet having 85% active ramsdellite material, 10% conductive carbon and 5% PVDF, was discharged to 1 V and charged back to 2 V under PEIS conditions as indicated in the experimental section. Impedance measurements were taken after 6 h voltage equilibration at different potentials. In the first discharge, very noisy spectra were recorded except for 1.2 V. On charge reliable data were obtained at 1.5, 1.7 and 2.0 V denoted as circles in the potentiostatic discharge-charge curve shown in Fig. S4.

The impedance response of the working electrode is very similar at every voltage. Fig. 9 shows the impedance obtained at 1.7 V, x = 0.272, as an example of the typical response. It shows both the experimental data and the fitted spectrum using the circuit model shown in the inset. This circuit is like the one described above for the fitting of the cycled two-electrode cell. However, although fitting has been made using such circuit with two RCPE, there is an overlapping of both elements due to close relaxation frequencies. Thus, caution must be exerted on the individual values. Hence, R2 + R3 values corresponding to $R_{int} + R_{ct}$ is better used for the analysis. In fact, in some cases (at 1.0 and 1.2 V, not shown) fitting can be made using only one RCPE. The resulting values obtained from the high and medium frequency range are listed in Table S2. They show that both R_e and $R_{int} + R_{ct}$ remain constant and very low in the whole 1–2 V voltage range.

The low frequency range has been modelled with a Warburg element. However, as the observed spike deviates from SILD towards finite space diffusion at the lowest frequencies a Warburg open-circuit element has been used. This behaves as a capacitor at the lowest frequencies due to charge accumulation as ions are blocked at the surface because diffusion cannot progress at such short time scale.

Nevertheless, lithium diffusion coefficient can be calculated from the frequency range data for which SILD is observed. Eq. 5, derived from Fick`s law of diffusion, can be used for such purpose [46]:

$$D_{Li^+} = \left(\frac{V_m}{zFA}\right)^2 \left(\frac{dE}{dx}\right)^2 \left(\frac{1}{\sqrt{2}\ m\sigma_w}\right)^2 \quad (5)$$

V_m is the molar volume of $LiFe_{0.125}Ti_{1.875}O_4$ that is assumed to remain nearly constant upon intercalation, z is the number of exchanged electrons in the redox reaction, F is the Faraday's constant, $A = 4.26\ cm^2\ mg^{-1}$ is the specific area determined by BET method on the pristine compound and also assumed to remain constant upon intercalation, $\frac{dE}{dx}$ is the slope of the tangent line to the E vs. x near-equilibrium curve at the x value for which impedance was measured, m is the electrode mass, and σ_W is the Warburg coefficient. This coefficient has been determined in the region where semi-infinite diffusion occurs in which Warburg impedance, Z_w, is expressed as in Eq. 6:

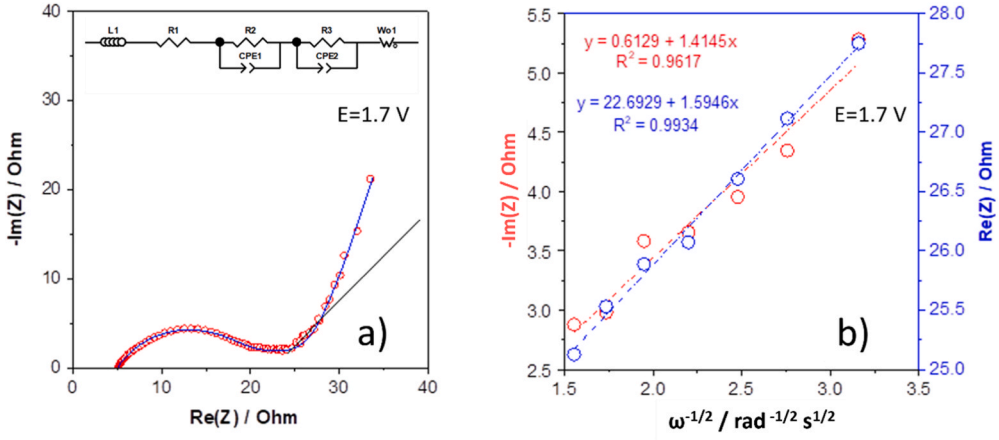

Fig. 9. Nyquist plots corresponding to the impedance of the working electrode of a three-electrode cell bearing $LiFe_{0.125}Ti_{1.875}O_4$ (composite 85:10:5) as the active material (a). The experimental data are shown as red circles while the solid blue line depicts the fitting to the equivalent circuit shown in the inset. The black solid line with slope= 1 is a guide for the eyes to visualize the region in which SILD condition is fulfilled. b) Warburg impedance, -Im(Z) and Re(Z) as a function of the angular frequency in the frequency range in which SILD is fulfilled.

$$Z_w = \frac{\sigma_w}{\sqrt{\omega}} - i\frac{\sigma_w}{\sqrt{\omega}} \quad (6)$$

where ω is the radial frequency. Therefore, under such conditions $Z' = -Z''$ as it happens in the frequency regions for which the experimental points of the Nyquist plot are aligned onto the black solid straight line depicted in Fig. 9a with slope= 1. Using this frequency range Warburg coefficient has been obtained from the slope of Z' *or* $-Z''$ vs. $\omega^{-1/2}$ (Fig. 9b) [47]. Because both representations should provide the same slope the average value has been taken (in the case shown in Fig. S4 $\sigma_W = 1.51$ ohm rad$^{1/2}$ s$^{-1/2}$ or 0.6 ohm s$^{-1/2}$) Note that in the example given in Fig. 9 the frequency region where Eq. 6 is fulfilled is very narrow as due to the transition to a finite length diffusion due to the accumulation of charge at the electrode surface (finite space) as mentioned above. The same was observed at any potential indicating limited diffusion in the whole intercalation range.

Table 6 shows the values of Warburg coefficient and other parameters used for determination of D_{Li+} at different voltages and the corresponding x values (marked with blue circles in the voltage composition curve shown in Fig. S4. Most data correspond to regions of the voltage composition curve where a steady change of voltage occurs because Eq. 5 cannot be applied in a region where a biphasic change takes place $\left(\frac{dE}{dx} = 0\right)$. However, data recorded at 1.5 V likely correspond to a composition (x = 0.4) very close to a two-phase region even although a flat voltage variation is not observed due to thermodynamic and kinetic effect. Hence, a non-zero slope can be read. Use of this value to determine diffusion coefficient provides the so called "apparent chemical diffusion coefficient" [48–50].

From the results it can be deduced that lithium diffusion is faster in the high voltage region (low lithium content) than in the low voltage range (high lithium content) with the diffusion coefficient being two orders of magnitude lower in the low voltage range. Worth mentioning that fully lithiated $Li_2Ti_2O_4$, obtained after full discharge of pristine $LiTi_2O_4$ through a two-phase transition, retains the ramsdellite structure as proved by *operando* synchrotron diffraction study [19]. Hence, assuming an identical structural scenario for Fe-substituted $LiFe_{0.125}Ti_{0.875}O_4$, increased occupancy of available Li^+ sites with stronger Li^+-Li^+ repulsions would explain more sluggish lithium diffusion at low voltage.

Table 6
Warburg coefficients and other parameters used for determination of D_{Li+}.

$Li_{1+x}Fe_{0.125}Ti_{0.875}O_4$	dE/dx V mol	σ_w Ω s$^{-1/2}$	D_{Li+} cm^2 s^{-1}
1.2 V (discharge) x = 0.916	-0.98	12.5	1.55×10^{-13}
1.5 V (charge) x = 0.371	-0.1	0.44	1.3×10^{-12} (apparent)
1.7 V (charge) x = 0.272	-2.32	0.6	3.8×10^{-10}
2.0 V (charge) x = 0.084	-1.63	0.6	1.87×10^{-10}

($V_m = 42.79$ cm^3 mol^{-1}; A = 4.26 cm^2 mg^{-1}; m = 14.64 mg)

3.4.2. *High voltage range. Charge from ocv to 4.5 V*

$LiTi_2O_4$ ramsdellite shows a single process upon charge to 4.5 V centered at 2.2 V vs. Li^+/Li, ascribed to the reversible $Ti^{3+/4+}$ pair, delivering a reversible capacity of 80 mAh g^{-1} (0.5 Li/f.u.) in good agreement with previous reports [8,20]. For Fe-substituted ramsdellites, first charge capacities are 100 mAh g^{-1} (x = 0.125), 40 mAh g^{-1} (x = 0.25), and 49 mAh g^{-1} (x = 0.5). The flat deinsertion potential in ramsdellite $LiTi_2O_4$ at ~2.2 V was ascribed to a two-phase domain within two narrow solid solutions at the beginning and the end of the biphasic region [19]. Interestingly, ramsdellite $LiFe_{0.125}Ti_{1.875}O_4$

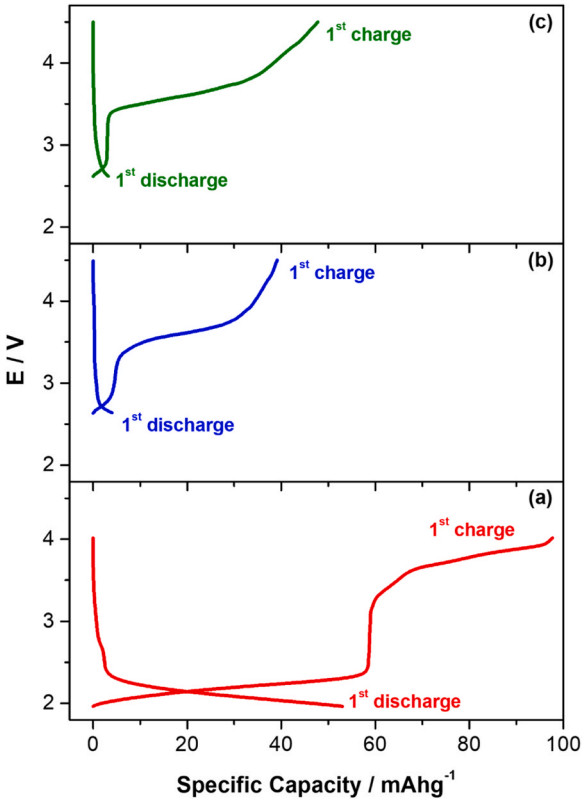

Fig. 10. Charge-discharge capacities of $LiFe_{0.125}Ti_{1.875}O_4$ (a), $LiFe_{0.25}Ti_{1.75}O_4$ (b), and $LiFe_{0.50}Ti_{1.50}O_4$ (c) ramsdellites upon charge to 4.5 V vs. Li^+/Li.

(Fig. 10a) exhibits the same flat charge curve at the same potential, hence associated with the $Ti^{3+/4+}$ pair. For both ramsdellites reversible capacity is clearly lower than the theoretical one based on 1 Ti^{3+} in $LiTi_2O_4$ (80 mAh g^{-1} vs. 161 mAh g^{-1}) and 0.7 Ti^{3+} in $LiFe_{0.125}Ti_{1.875}O_4$ (60 mAh g^{-1} vs. 113 mAh g^{-1}), denoting some hindrance of lithium deinsertion. This becomes more noticeable as iron content increases (Fig. 10b and c) for which a pronounced diminution in the process at 2.2 V is observed. In contrast to undoped $LiTi_2O_4$, all Fe-doped ramsdellites exhibit a second charge process at higher 3.5 – 4.0 V (Fig. 9). This high-voltage process could in principle be attributable to the $Fe^{3+/4+}$ redox pair, although absence of the corresponding high potential process during the following discharge curve testifies to irreversibility. Moreover, electrolyte decomposition could also account for irreversibility at higher potential. Note that $Fe^{2+/3+}$ oxidation has not been considered due to the low Fe^{2+}content in all studied Fe-doped ramsdellites (0.02 – 0.08 Fe^{2+}/f.u.). On the other hand, for ramsdellite $LiFe_{0.125}Ti_{1.875}O_4$ first charge capacity developed in the 3.5–4.0 V range clearly exceeds that of the one calculated from available Fe^{3+} (37 mAh g^{-1} vs. 7 mAh g^{-1}).

To clarify whether the high-potential process is related to (oxidation of) Fe^{3+} of the ramsdellite or side reactions such as electrolyte decomposition, *operando* X-ray diffraction measurements were conducted during a full charge-discharge cycle in the 2.0 – 4.5 V range. The evolution of XRD patterns of $LiTi_{1.875}Fe_{0.125}O_4$ in the whole angular range upon oxidation to 4.5 V and further reduction to 2.0 V is shown in Fig. S5. To better illustrate changes, Fig. 11 collects the evolution of 110 and 130 diffraction peaks of the ramsdellite structure. It is clearly seen that charge to ~3.0 V produces a shift of *hk*0 reflections towards higher angles, in connection with a decrease of both *a* and *b* axis, indicating transition to a higher oxidation state of titanium, in agreement with previous reports [19,20,30]. By means of higher resolution synchrotron X-ray diffraction conducted *in operando* it was shown that the apparent single-phase lithium deinsertion (as one might infer from the continuous shift of diffraction maxima observed in Fig. 11) actually consists of a two-phase region of two closely related ramsdellite structures [19]. The overall small changes in lattice parameters upon (de-)insertion of lithium in the ocv-4.5 V range $\Delta a/a = -1.20\%$, $\Delta b/b = -1.15\%$, $\Delta c/c = +0.12\%$, and $\Delta V/V = +2.13\%$ are a clear proof of the robustness of the ramsdellite structure for lithium (de-)insertion. However, no significant changes regarding either position or intensity of diffraction maxima are observed upon further charging above 3 V and to the maximum voltage investigated, 4.5 V. Thus, it can be concluded that lithium deinsertion and concomitant oxidation of Fe^{3+} was not possible in Fe-doped ramsdellite phase to the maximum potential studied (4.5 V). On the other hand, the progressive retrogression of diffraction maxima when discharged to 2 V nicely proves the reversibility of the $Ti^{4+/3+}$ redox pair in the lower voltage range (2.2 V). The evolution of cell parameters during the full charge-discharge cycle are portrayed in Fig. 12.

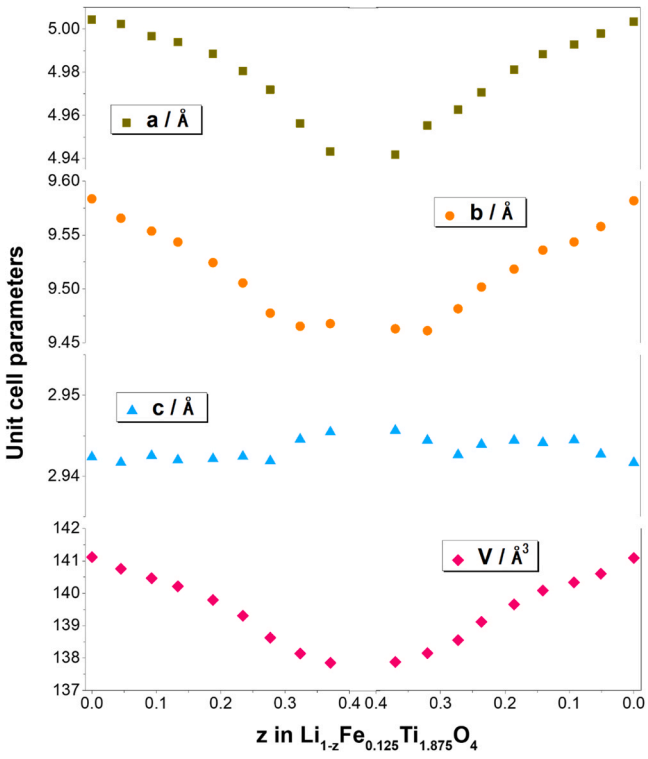

Fig. 12. Evolution of cell parameters *a*, *b* and *c* and the cell volume during a full charge-charge cycle in the 2.0–4.5 V range.

4. Conclusions

In conclusion, iron substituted ramsdellites $LiFe_xTi_{2-x}O_4$ are successfully obtained in the compositional range $0 \leq x \leq 0.5$ by the high temperature ceramic method.

^{57}Fe Mössbauer spectra allowed to discern between Fe^{2+} and Fe^{3+}, both octahedrally coordinated in the framework of the ramsdellite

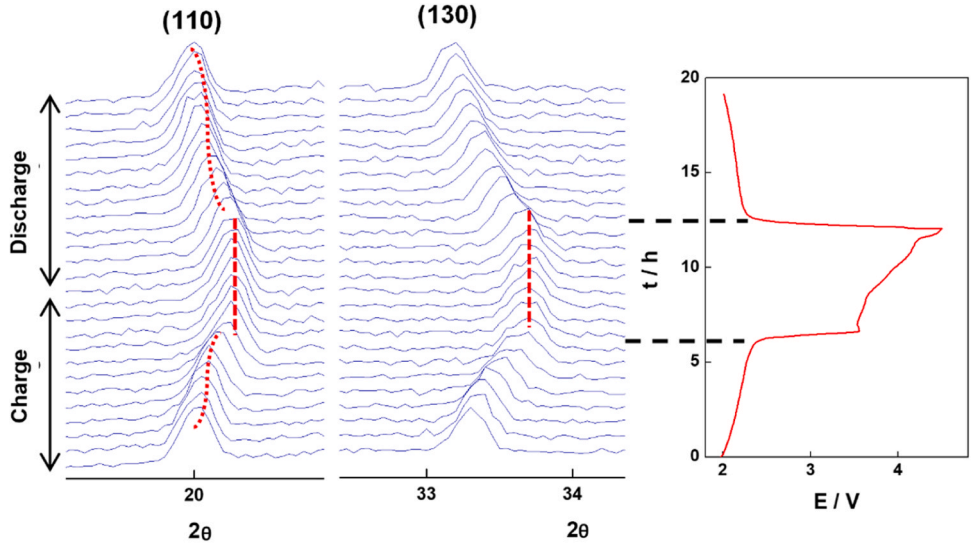

Fig. 11. Evolution of 110 and 130 reflections of ramsdellite $LiTi_{1.875}Fe_{0.125}O_4$ upon charge to 4.5 V and further discharge to 2 V.

structure.

The electrochemical results showed that introduction of low iron content improved the electrochemical behavior as compared to undoped $LiTi_2O_4$. From galvanostatic discharge/charge curves, the contribution to the total capacity for iron substituted specimens in the low voltage zone, *ocv* to 1 V, is much higher than in the high voltage range, *ocv* to 4.5 V. The outstanding and outperforming electrochemical properties of $LiFe_{0.125}Ti_{1.875}O_4$: extended capacity and improved cyclability at high current rates, are ascribable to: 1) two active redox pairs, Ti^{4+}/Ti^{3+} and Fe^{3+}/Fe^{2+}; 2) a higher amount of available Ti^{4+} ions; 3) a high lithium diffusion coefficient at higher potentials in the low voltage range ($\sim 10^{-10}$ cm^2 s^{-1}) with stable interfaces, and 4) better electrical properties due to the presence of metallic iron, boosting farther electronic conductivity in $LiFe_{0.125}Ti_{1.875}O_4$. This allowed an attractive lithium storage capacity of up to 180 mAh g^{-1} at low current of C/30 (5.3 mA g^{-1}) and a still noticeable capacity of 71 mAh g^{-1} at high current of 2 C (320 mA g^{-1}). Moreover, ramsdellites with higher iron content showed clear signature of reversible Fe^{3+}/Fe^{2+} redox couple, in contrast to other related iron substituted titanate ramsdellites, in which irreversible capacities related to Fe^{3+}/Fe^{2+} redox couple were found. The surprising reversible Fe^{3+}/Fe^{2+} redox couple in this work may therefore draw a path to designing high-capacity electrodes with reversible multi-metal electron transfer using earth abundant and environmental benign iron and titanium element sources for building high energy and power density lithium batteries. However, there is need to improve the electrochemical behavior of iron substituted titanate ramsdellites in the high voltage range (ocv-4.5 V), where contribution to total capacity is limited except for $LiFe_{0.125}Ti_{1.875}O_4$. Moreover, the significant irreversible capacity developed in the high voltage range, attributed to electrolyte decomposition as shown by operando XRD would have to be addressed to unlock potential availability of reversible Fe^{3+}/Fe^{4+} redox couple improving farther lithium storage ability.

CRediT authorship contribution statement

Pilar Díaz-Carrasco: Methodology, Validation, Formal analysis, Investigation, Resources, Visualization. **Alois Kuhn:** Investigation, Conceptualization, Methodology, Resources, Writing – Original Draft, Writing – Review & Editing, Supervision. **Nieves Menéndez:** Validation, Formal analysis, Investigation, Visualization, Writing – Original Draft. **Flaviano García-Alvarado:** Investigation, Conceptualization, Writing- Original Draft, Supervision, Project Administration, Funding acquisition.

Declaration of Competing Interest

The authors declare that they have no known competing financial interests or personal relationships that could have appeared to influence the work reported in this paper.

Data Availability

Data will be made available on request.

Acknowledgments

We thank MICIN/AEI/10.103039/501100011033 for funding the projects PID2019–106662RB-C41, PID2021–123431OB-I00 and PID2022-139039OB-C21. Financial support from Universidad CEU San Pablo is also acknowledged. We also thank Central Services (SCAI) of University of Málaga for the BET measurements.

Appendix A. Supporting information

Supplementary data associated with this article can be found in the online version at doi:10.1016/j.jallcom.2023.172027.

References

[1] X. Chen, Y. Huang, K. Zhang, X. Feng, M. Wang, Porous TiO2 nanobelts coated with mixed transition-metal oxides Sn3O4 nanosheets core-shell composites as high-performance anode materials of lithium ion batteries, Electrochim. Acta 259 (2018) 131–142.
[2] Z. Li, H. Zhao, P. Lv, Z. Zhang, Y. Zhang, Z. Du, Y. Teng, L. Zhao, Z. Zhu, Watermelon-Like structured SiOx–TiO2@C nanocomposite as a high-performance lithium-ion battery anode, Adv. Funct. Mater. 28 (2018), 1605711.
[3] M. Zheng, H. Tang, L. Li, Q. Hu, L. Zhang, H. Xue, H. Pang, Hierarchically nanostructured transition metal oxides for lithium-ion batteries, Adv. Sci. 5 (2018), 1700592.
[4] C. Han, D. Yang, Y. Yang, B. Jiang, Y. He, M. Wang, A.-Y. Song, Y.-B. He, B. Li, Z. Lin, Hollow titanium dioxide spheres as anode material for lithium ion battery with largely improved rate stability and cycle performance by suppressing the formation of solid electrolyte interface layer, J. Mater. Chem. A 3 (2015) 13340–13349.
[5] Y.-S. Hu, L. Kienle, Y.-G. Guo, J. Maier, High lithium electroactivity of nanometer-sized rutile TiO2, Adv. Mater. 18 (2006) 1421–1426.
[6] P. Díaz-Carrasco, A. Duarte-Cárdenas, A. Kuhn, F. García-Alvarado, Understanding the high performance of nanosized rutile TiO2 anode for lithium-ion batteries, J. Power Sources 515 (2021), 230632.
[7] M.T. Gutierrez-Florez, A. Kuhn, F. Garcia-Alvarado, Lithium intercalation in KxTi8O16 compounds, Int. J. Inorg. Mater. 1 (1999) 117–121.
[8] A. Kuhn, R. Amandi, F. Garcia-Alvarado, Electrochemical lithium insertion in TiO2 with the ramsdellite structure, J. Power Sources 92 (2001) 221–227.
[9] Y. Tang, Y. Zhang, J. Deng, J. Wei, T. Hong Le, B.K. Chandran, Z. Dong, Z. Chen, X. Chen, Mechanical force-driven growth of elongated bending TiO2-based nanotubular materials for ultrafast rechargeable lithium ion batteries, Adv. Mater. 26 (2014) 6111–6118.
[10] T. Ohzuku, A. Ueda, N. Yamamoto, Zero-Strain Insertion Material of Li [Li1 / 3Ti5 / 3] O 4 for Rechargeable Lithium Cells, J. Electrochem. Soc. 142 (1995) 1431–1435.
[11] M. deDompablo, E. Moran, A. Varez, F. GarciaAlvarado, Electrochemical lithium intercalation in Li2Ti3O7-ramsdellite structure, Mater. Res. Bull. 32 (1997) 993–1001.
[12] Y. Wang, W. Zhu, Micro/nano-structured Li4Ti5O12 as high rate anode material for lithium ion batteries, Solid State Ion. 349 (2020), 115297.
[13] R.A. Hernández-Carrillo, G. Ramos-Sánchez, G. Guzmán-González, N.A. García-Gomez, I. González, E.M. Sanchez-Cervantes, Synthesis and characterization of iron − doped Li4Ti5O12 microspheres as anode for lithium-ion batteries, J. Alloy. Compd. 735 (2018) 1871–1877.
[14] Yan, L. (Yan, Lv); Qin, JM (Qin, Jieming); Liang, BK (Liang, Benkuan); Gao, SL (Gao, Shanlin); Wang, B (Wang, Bo); Cui, JY (Cui, Jiuyue); Bolag, A (Bolag, Altan); Yang, YC (Yang, Yanchun), High Pressure Rapid Synthesis of LiCrTiO4 with Oxygen Vacancy for High Rate Lithium-Ion Battery Anodes, Small, 18 (2022) 2202901.
[15] Zhu, C.X. (Zhu, Caixia); Tang, YK (Tang, Yakun); Liu, L (Liu, Lang); Li, XH (Li, Xiaohui); Gao, Y (Gao, Yang); NuLi, YN (NuLi, Yanna), LiCrTiO4 Nanowires as High-Performance Cathodes for Magnesium-Lithium Hybrid Batteries, ACS Sustainable Chemistry & Engineering, 7 (2019) 14539–14544.
[16] M.H. Wang, Z. Ma, H.-G. Xue, S.P. Guo, LiFeTiO4/CNTs composite as a cathode material with high cycling stability for lithium-ion batteries, Inorganic Chemistry, Frontier 5 (2019) 2306–2313.
[17] M.B. Vazquez-Santos, P. Tartaj, E. Morales, J.M. Amarilla, TiO2 nanostructures as anode materials for Li/Na-ion batteries, Chem. Rec. 18 (2018) 1178–1191.
[18] S. Lou, Y. Zhao, J. Wang, G. Yin, C. Du, X. Sun, Ti-based oxide anode materials for advanced electrochemical energy storage: lithium/sodium ion batteries and hybrid pseudocapacitors, Small 15 (2019), 1904740.
[19] A. Kuhn, C. Baehtz, F. Garcia-Alvarado, Structural evolution of ramsdellite-type LixTi2O4 upon electrochemical lithium insertion–deinsertion ($0 \leq x \leq 2$), J. Power Sources 174 (2007) 421–427.
[20] R.K.B. Gover, J.R. Tolchard, H. Tukamoto, T. Murai, J.T.S. Irvine, Investigation of ramsdellite titanates as possible new negative electrode materials for Li batteries, J. Electrochem. Soc. 146 (1999) 4348–4353.
[21] R. Kanazawa, M. Haruta, T. Doi, M. Inaba, Preparation and charge/discharge characteristics of carbon-modified ramsdellite TiO2 as a high potential anode, Electrochemistry 83 (2015) 867–869.
[22] A. Kuhn, M. Martin, F. Garcia-Alvarado, New ramsdellites LiTi2-yVyO4 ($0 \leq y \leq 1$): synthesis, structure, magnetic properties and electrochemical performances as electrode materials for lithium batteries, J. Solid State Chem. 183 (2010) 20–26.
[23] A. Kuhn, M. Martin, F. Garcia-Alvarado, Synthesis, structure and electrochemical lithium intercalation chemistry of ramsdellite-type LiCrTiO4, Z. Fur Anorg. Und Allg. Chem. 634 (2008) 880–886.
[24] J.C. Pérez-Flores, M. Hoelzel, F. García-Alvarado, A. Kuhn, Structural and electrochemical study of vanadium-doped tio2 ramsdellite with superior lithium storage properties for lithium-ion batteries, ChemPhysChem 17 (2016) 1062–1069.
[25] A. Kuhn, P. Diaz-Carrasco, M. de Dompablo, F. Garcia-Alvarado, On the synthesis of ramsdellite LiTiMO4 (M = Ti, V, Cr, Mn, Fe): an experimental and computational study of the spinel–ramsdellite transformation, Eur. J. Inorg. Chem. 21 (2007) 3375–3384.
[26] R.K.B. Gover, J.T.S. Irvine, A.A. Finch, Transformation of LiTi2O4from Spinel to Ramsdellite on Heating, J. Solid State Chem. 132 (1997) 382–388.
[27] G. Avdeev, K. Petrov, I. Mitov, X-ray diffraction and Mössbauer spectroscopy studies of LiFe0.5Ti1.5O4 – a new primitive cubic ordered spinel, Solid State Sci. 9 (2007) 1135–1139.

[28] J. Rodríguez-Carvajal, Recent advances in magnetic structure determination by neutron powder diffraction, Phys. B 192 (1993) 55–69.
[29] M. Morcrette, Y. Chabre, G. Vaughan, G. Amatucci, J.B. Leriche, S. Patoux, C. Masquelier, J.M. Tarascon, In situ X-ray diffraction techniques as a powerful tool to study battery electrode materials, Electrochim. Acta 47 (2002) 3137–3149.
[30] R.A. Brand, Improving the validity of hyperfine field distributions from magnetic alloys: Part I: Unpolarized source, Nucl. Instrum. Methods Phys. Res. Sect. B: Beam Interact. Mater. At. 28 (1987) 398–416.
[31] J. Akimoto, Y. Gotoh, M. Sohma, K. Kawaguchi, Y. Oosawa, H. Takei, Synthesis and crystal structure of ramsdellite-Type Li0.5TiO2, J. Solid State Chem. 110 (1994) 150–155.
[32] S. Scharner, W. Weppner, P. Schmid-Beurmann, Cation distribution in ordered spinels of the Li2O–TiO2–Fe2O3System, J. Solid State Chem. 134 (1997) 170–181.
[33] A. Deschanvres, B. Raveau, Z. Sekkal, Mise en evidence et etude cristallographique d′une nouvelle solution solide de type spinelle Li1+xTi2−xO4 0 ⩽ x ⩽ 0, 333, Mater. Res. Bull. 6 (1971) 699–704.
[34] R.D. Shannon, Revised effective ionic radii and systematic studies of interatomic distances in halides and chalcogenides, Acta Crystallogr. Sect. A: Cryst. Phys. Diffr. Theor. Gen. Crystallogr. 32 (1976) 751–767.
[35] J. Akimoto, Y. Gotoh, Y. Oosawa, N. Nonose, T. Kumagai, K. Aoki, H. Takei, Topotactic oxidation of ramsdellite-type Li0.5TiO2, a new polymorph of titanium dioxide: TiO2(R), J. Solid State Chem. 113 (1994) 27–36.
[36] R.K.B. Gover, J.T.S. Irvine, A. New, Solid solution series linking LiTi2O4 and Li2Ti3O7ramsdellites: a combined x-ray and neutron study, J. Solid State Chem. 141 (1998) 365–372.
[37] J. Panda, U.P. Singh, R. Sahu, Synthesis, characterization of TiO2 nano particles for enhancement of electron transport application in DSSC with Cu-BPCA Dye, IOP Conf. Ser.: Mater. Sci. Eng. 410 (2018) 012008.
[38] V. Vetrivel, K. Rajendran, V. Kalaiselvi, Synthesis and characterization of Pure Titanium dioxide nanoparticles by Sol- gel method, Int. J. Chem. Tech. Res. 7 (2014-2015) 1090–1097.
[39] A. León, P. Reuquen, C. Garín, R. Segura, P. Vargas, P. Zapata, P.A. Orihuela, FTIR and Raman characterization of TiO2, nanoparticles coated with polyethylene glycol as carrier for 2-methoxyestradiol, Appl. Sci. 7 (2017) 49.
[40] S. Mugundan, B. Rajamannan, G. Viruthagiri, N. Shanmugam, R. Gobi, P. Praveen, Synthesis and characterization of undoped and cobalt-doped TiO2 nanoparticles via sol–gel technique, Appl. Nanosci. 5 (2015) 449–456.
[41] L. Aldon, P. Kubiak, A. Picard, P.E. Lippens, J. Olivier-Fourchade, J.-C. Jumas, Mössbauer spectrometry as a powerful tool to study lithium reactivity mechanisms for battery electrode materials, Hyperfine Interact. 156/157 (2004) 497–503.
[42] M.C. López, G.F. Ortiz, P. Lavela, J.L. Tirado, R. Stoyanova, E. Zhecheva, Tunable Ti4+/Ti3+ redox potential in the presence of iron and calcium in NASICON-type related phosphates as electrodes for lithium batteries, Chem. Mater. 25 (2013) 4025–4035.
[43] S.H. Ma, H. Noguchi, Preparation of Fe doped Li2Ti3O7 and its electrochemical properties, Electrochemistry 69 (2001) 526–529.
[44] A.D. Robertson, H. Tukamoto, J.T.S. Irvine, Li1+xFe1−3xTi1+2xO4 (0.0 ≤ x ≤ 0.33) based spinels: possible negative electrode materials for future Li-ion batteries, J. Electrochem. Soc. 146 (1999) 3958–3962.
[45] I. Tsuyumoto, T. Moriguchi, Synthesis and lithium insertion properties of ramsdellite LixTiO2 anode materials, Mater. Res. Bull. 70 (2015) 748–752.
[46] C. Ho, I.D. Raistrick, R.A. Huggins, Application of A-C techniques to the study of lithium diffusion in tungsten trioxide thin films, J. Electrochem Soc. 127 (1980) 343–350.
[47] J. Kaspar, M. Graczyk-Zajac, R. Riedel, Determination of the chemical diffusion coefficient of Li-ions in carbon-rich silicon oxycarbide anodes by electro-analytical methods, Electrochim. Acta 115 (2014) 665–670.
[48] B. Babu, M.M. Shaijumon, Studies on kinetics and diffusion characteristics of lithium ions in TiNb2O7, Electrochim. Acta 345 (2020), 136208.
[49] Y. Zhu, T. Gao, X. Fan, F. Han, C. Wang, Electrochemical techniques for intercalation electrode materials in rechargeable batteries, Acc. Chem. Res. 50 (2017) 1022–1031.
[50] X.H. Rui, N. Ding, J. Liu, C. Li, C.H. Chen, Analysis of the chemical diffusion coefficient of lithium ions in Li3V2(PO4)3 cathode material, Electrochim. Acta 55 (2010) 2384–2390.